Quarterly Reviews of Biophysics

cambridge.org/qrb

Current limitations to high-resolution structure determination by single-particle cryoEM

Edoardo D'Imprima* and Werner Kühlbrandt

Department of Structural Biology, Max Planck Institute of Biophysics, Frankfurt am Main, Max von Laue Strasse 3, 60438, Germany

Review

*Current Address: Structural and Computational Biology Unit, European Molecular Biology Laboratory, Meyerhofstrasse 1, 69117 Heidelberg, Germany.

Cite this article: D'Imprima E, Kühlbrandt W (2021). Current limitations to high-resolution structure determination by single-particle cryoEM. *Quarterly Reviews of Biophysics* **54**, e4, 1–15. https://doi.org/10.1017/S0033583521000020

Received: 24 August 2020
Revised: 20 January 2021
Accepted: 29 January 2021

Keywords:
Air-water interface; beam-induced movement; CryoEM; electron cryo-microscopy; sample preparation; structure of macromolecular complexes

Author for correspondence:
Werner Kühlbrandt,
Email: werner.kuehlbrandt@biophys.mpg.de

Abstract

CryoEM has become the method of choice for determining the structure of large macromolecular complexes in multiple conformations, at resolutions where unambiguous atomic models can be built. Two effects that have limited progress in single-particle cryoEM are (i) beam-induced movement during image acquisition and (ii) protein adsorption and denaturation at the air-water interface during specimen preparation. While beam-induced movement now appears to have been resolved by all-gold specimen support grids with very small holes, surface effects at the air-water interface are a persistent problem. Strategies to overcome these effects include the use of alternative support films and new techniques for specimen deposition. We examine the future potential of recording perfect images of biological samples for routine structure determination at atomic resolution.

Table of contents

Introduction 1

Beam-induced movement 1

All-gold support foils with sub-µm holes 3

Protein adsorption to the air-water interface 5

Improving sample quality 5

Continuous support films 6

New methods of sample deposition 7

Conclusion and outlook 10

Introduction

Single-particle electron cryo-microscopy (cryoEM) has developed into a technique for determining the structure of protein complexes at high resolution, at a rate that was difficult to imagine at the outset of the resolution revolution only a few years ago (Kühlbrandt, 2014). The quality of cryoEM structures rivals (Ben-Shem *et al.*, 2011), or even surpasses (Safarian *et al.*, 2019) those obtained by X-ray crystallography. For a detailed description of the cryoEM method, we refer to recent reviews (Cheng *et al.*, 2015; Vinothkumar and Henderson, 2016; Mills, 2021). Apart from radiation damage, which is the primary and fundamental limitation in cryoEM of radiation-sensitive biological samples, two factors have limited the rate of progress towards even better structures and even wider application of single-particle cryoEM: (i) beam-induced specimen movement and (ii) protein adsorption to the air-water interface. This review examines current strategies to overcome these effects.

Beam-induced movement

Specimens for cryoEM are prepared by plunge-freezing (Dubochet *et al.*, 1982, 1988), whereby a few microliters of sample solution in aqueous buffer are spread on a 3 mm EM support grid usually coated with holey carbon film[1]. Excess solution is blotted off with filter paper to leave a thin layer of liquid that stretches across the holes in the carbon film. The total volume of the aqueous layer is typically much less than 0.01% of the volume applied. Upon plunging into

[1]For the purpose of this review, we refer to the 3 mm metal mesh of the specimen support as 'grid', the amorphous or holey carbon (or graphene) film on the grid as 'film', and the thin layer of liquid or vitreous water in the holes or on the film as 'layer'.

© The Author(s), 2021. Published by Cambridge University Press. This is an Open Access article, distributed under the terms of the Creative Commons Attribution licence (http://creativecommons.org/licenses/by/4.0/), which permits unrestricted re-use, distribution, and reproduction in any medium, provided the original work is properly cited.

CAMBRIDGE UNIVERSITY PRESS

liquid ethane, the aqueous layer cools from room temperature to ~90 K in less than 0.1 ms (Dubochet *et al.*, 1988). At this high cooling rate, the water molecules do not have time to form ice crystals, and the liquid layer freezes into a glass-like amorphous solid. Under normal laboratory conditions, the maximum thickness of aqueous layers that can be vitrified is ~1 µm (Studer *et al.*, 2008). The mean free path of 300 kV electrons in carbon or water is ~300 nm (Glaeser *et al.*, 2016), and this places an upper thickness limit on biological samples for transmission electron microscopy. Thinner vitrified layers (~30 nm or 300 Å) are preferable, because they give higher image contrast and better resolution.

Beam-induced specimen movement during image acquisition (Fig. 1) is an insidious problem that has long prevented routine determination of macromolecular structures at atomic or near-atomic resolution by cryoEM (Henderson and Glaeser, 1985; Glaeser *et al.*, 2011; Henderson *et al.*, 2011; Brilot *et al.*, 2012; Campbell *et al.*, 2012). It is most likely caused by the release of mechanical strain frozen into the glass-like, unsupported layer of vitrified water upon exposure to the electron beam (Glaeser *et al.*, 2016; Vinothkumar and Henderson, 2016). Electrostatic charge building up on the non-conductive cryo-specimen during electron irradiation, which has been suggested as an alternative or contributing cause (Downing *et al.*, 2004), is insignificant by comparison (Russo and Henderson, 2018*a*, 2018*b*).

Rapid freezing traps mechanical stress in the layer of vitrified buffer (Fig. 2). When plunged into liquid ethane, the sample solution in the holes of the support film freezes and expands to lower-density vitreous water, while the support film itself contracts (Glaeser *et al.*, 2016). As a result, the water layer in the hole buckles and forms a shallow dome, depending on the dimensions and geometry of the hole (Fig. 2*a*) (Naydenova *et al.*, 2020). The direction in which the layer domes or buckles appears to be random. When the vitrified layer is irradiated with electrons for cryoEM data collection (typically at ~84 K if the microscope is cooled with liquid nitrogen), the glass-like solid turns into viscous liquid (McMullan *et al.*, 2015). Mechanical stress is released, and the vitrified layer in the hole performs a drumhead motion. The direction of movement is the same as during freezing, resulting in a slightly more pronounced dome (Fig. 2*b*). This is evident from the direction of movement during electron exposure because, in projection, the particles on average appear to move away from the centre of the imaged area (Fig. 3*a*). During a 30 e A^{-2} exposure, virus particles in a thin layer of vitrified solution move by up to 60 Å and rotate by up to 5° (Brilot *et al.*, 2012) (Fig. 1). The linear movement is seen most easily when the specimen is tilted (Fig. 3*b*).

Beam-induced movement of cryoEM specimens occurs in two phases (Fig. 4) (Russo and Passmore, 2014*b*; Pfeil-Gardiner *et al.*, 2019). The initial phase is characterized by a burst-like motion, as the first electrons hit the specimen, releasing the stress trapped in the vitreous layer, and the doming becomes more pronounced. Movements in this early phase are up to five times higher than in the second phase, where moderate, continuous beam-induced motion probably results from the accumulation of new stress in the specimen, due to the breakage of covalent bonds and mass loss caused by radiation damage (Glaeser *et al.*, 2011; Glaeser, 2016; Naydenova *et al.*, 2020). Surprisingly, the movement in both phases is worse by a factor of two or more for samples cooled with liquid helium to around 4–17 K, rather than with liquid nitrogen to 84 K (Fig. 4*a*) (Pfeil-Gardiner *et al.*, 2019). For 2D crystals, cooling with liquid helium is known to reduce radiation damage by roughly a factor of two (Kühlbrandt *et al.*, 1994; Stark *et al.*, 1996). It would be excellent if we could take advantage of this extra cryoprotection factor for single particles as well, but at present, the massive beam-induced movement observed with non-crystalline, unsupported particles (Pfeil-Gardiner *et al.*, 2019) counteracts and obliterates the potential beneficial effect of helium cooling. Once this puzzling problem is resolved, liquid helium cooling should improve the signal-to-noise ratio of low-dose single-particle images just as much as for 2D crystals.

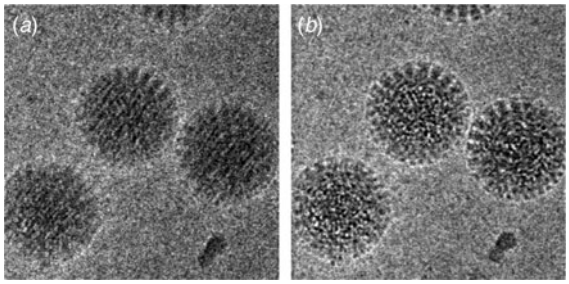


Fig. 1. Beam-induced movement of rotavirus particles. (*a*) Average of 60 movie frames indicates image blurring caused by beam-induced motion. High-resolution information is lost due to the ~60 Å displacement of particles during image acquisition. (*b*) Average of the same 60 frames after translational alignment. The contrast is substantially improved, with details at a higher resolution that are not visible in A (Brilot *et al.*, 2012).

Measurements of radiation damage with 300 kV electrons at liquid nitrogen temperature indicate a damage rate (expressed as a B factor) of ~5 $Å^2$ for every e $Å^{-2}$, both for single particles (Grant and Grigorieff, 2015) and 2D crystals (Peet *et al.*, 2019*b*). There is no reason why at liquid helium temperature, single particles and 2D crystals should behave differently. Earlier measurements with 2D bacteriorhodopsin crystals (purple membrane) at liquid nitrogen temperature (Stark *et al.*, 1996) had suggested a damage rate that was several times higher, which however appears to be an outlier (Naydenova *et al.*, 2020).

When cryoEM images are recorded as movie stacks with a direct electron detector, beam-induced movement can in principle be corrected by aligning successive movie frames (Brilot *et al.*, 2012; Campbell *et al.*, 2012; Ripstein and Rubinstein, 2016). The first few frames, at a cumulative dose of ~3–4 e $Å^{-2}$, are the least affected by radiation damage and therefore contain the most valuable high-resolution information. Due to the low electron exposure, the signal-to-noise ratio in all frames is poor, and therefore beam-induced particle movements are difficult to trace. These movements are particularly large in the first few frames. In early studies, the initial frames were simply discarded (Liao *et al.*, 2013; Allegretti *et al.*, 2014; Vinothkumar *et al.*, 2014). A better option is to down-weight the first few frames by an appropriate B factor, which is what all current image processing packages do (Grigorieff *et al.*, 2017; Punjani *et al.*, 2017; Zheng *et al.*, 2017; Zivanov *et al.*, 2018). Beam-induced movement – unlike macroscopic mechanical movement, caused e.g. by stage drift – happens on a time scale of pico- or nanoseconds (Guo *et al.*, 2020). Therefore, even the fastest and most sensitive detectors (Sun *et al.*, 2020), including any that may be developed in future, are unlikely to keep track of such very rapid movements with images that would necessarily be recorded at an extremely low dose and correspondingly low signal-to-noise ratio.

In principle, the mechanical stress trapped in the vitreous layer should be released upon devitrification. Devitrification converts solid vitreous water into thermodynamically metastable, but

https://doi.org/10.1017/S0033583521000020 Published online by Cambridge University Press

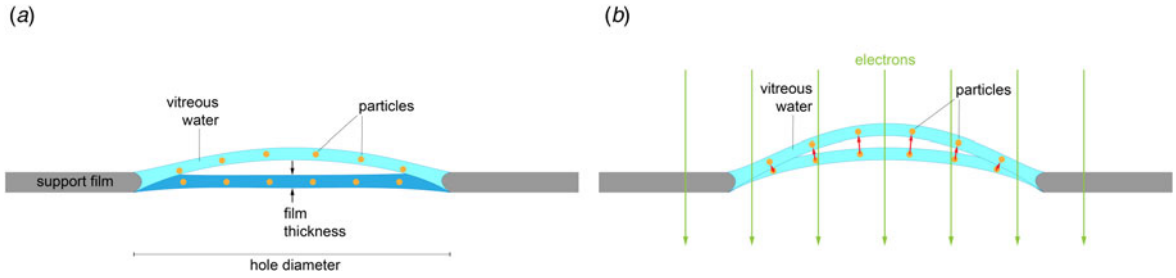


Fig. 2. Doming of a solid water layer on a cryoEM specimen support. (*a*) Thin layers of solid water used in cryoEM buckle during vitrification. Dark blue, liquid layer before vitrification; light blue, domed vitrified layer. (*b*) Electron irradiation causes the vitreous layer to move in the direction in which it buckled upon freezing, as evident from the correlated particle movement at the beginning of irradiation (see Fig. 3). Adapted from Naydenova *et al.*, (2020).

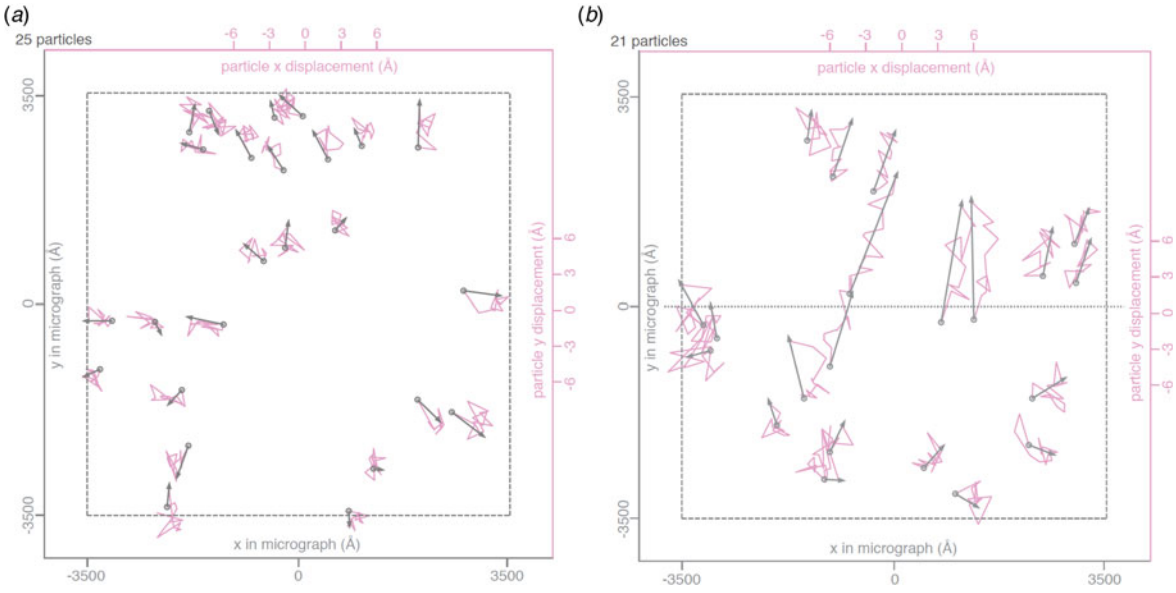


Fig. 3. Beam-induced movement of gold particles. Gold particle trajectories in a layer of vitrified water in 840 nm holes of an all-gold specimen support at 0° (*a*) and 30° tilt (*b*). Grey arrows indicate total displacement within the first 20 $e^{-} A^{-2}$ of irradiation. The trajectories are expanded 200x. Dashed line – imaged area; dotted line – direction of tilt axis (Naydenova *et al.*, 2020).

mechanically stable microcrystalline cubic ice. It is achieved by carefully warming the sample above the devitrification point at 143 K. Devitrification has been shown to preserve high-resolution detail in biological specimens (Cyrklaff and Kühlbrandt, 1994). Indeed, movies of protein particles in devitrified cryo-specimens indicate that beam-induced motion is reduced by a factor of ~4 in the first phase of rapid movement, and by a factor of 2 in the subsequent slower phase (Fig. 4*b*) (Wieferig *et al.*, 2021). A theoretical analysis of beam-induced movement based on heat transfer rates during cooling (Thorne, 2020) makes a number of suggestions of how the movement can be reduced, e.g. by appropriate choice of materials for the grid and support film. Unfortunately, controlled devitrification is not feasible in the column of high-end electron cryo-microscopes that are currently available, and devitrification outside the column vacuum entails a high risk of ice contamination.

All-gold support foils with sub-µm holes

Recently introduced all-gold cryoEM grid supports with very small holes appear to all but eliminate the long-standing problem of beam-induced specimen movement. Stable all-gold grids with standard-sized, 1.2–2 µm holes are known to reduce the movement induced by the electron beam by 40–80% (Russo and Passmore, 2014*b*). Progressively smaller holes were found to result in correspondingly smaller movements. At a hole diameter of around 250 nm, beam-induced movement all but disappeared. On this basis, new all-gold grids, referred to as 'HexAuFoil' (Fig. 5), have been developed (Naydenova *et al.*, 2020). HexAuFoils are arrays of 180–300 nm holes on a hexagonal lattice to maximize the transparent area. The new grids reduce beam-induced particle movement to less than 1 Å – about the diameter of a hydrogen atom – in a 30 e A^{-2} movie (Fig. 6). The movement depends on the extent to which the vitreous water layer buckles or domes, which in turn depends on its thickness and the hole diameter. Theoretical considerations indicated that doming should become insignificant at an aspect ratio of 11:1 (hole diameter to ice layer thickness) or less, and Russo and colleagues have demonstrated experimentally that this is in fact the case. With a vitreous water layer thickness of 300 Å that is e.g. desirable for 200 Å particles, the maximum hole diameter for

https://doi.org/10.1017/S0033583521000020 Published online by Cambridge University Press

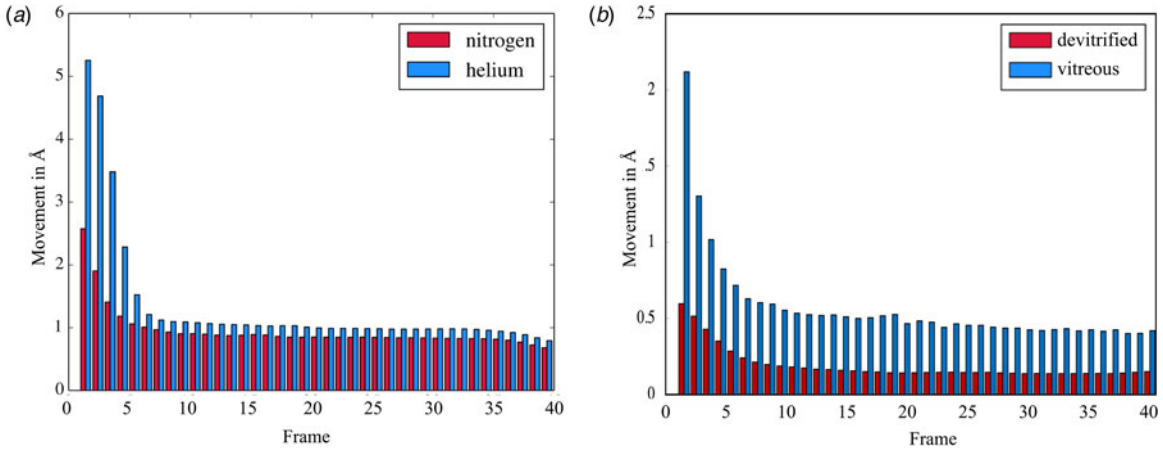


Fig. 4. Beam-induced movement of protein complexes. (*a*) Histogram of averaged per-frame particle movements in apoferritin specimens cooled with liquid nitrogen to 85 K (red) or liquid helium to 17 K (Pfeil-Gardiner *et al*., 2019). (*b*) Averaged beam-induced per-frame particle movements of alcohol oxidase particles in vitrified (blue) and devitrified (orange) layers of solid water. Adapted from Wieferig *et al*. (2021).

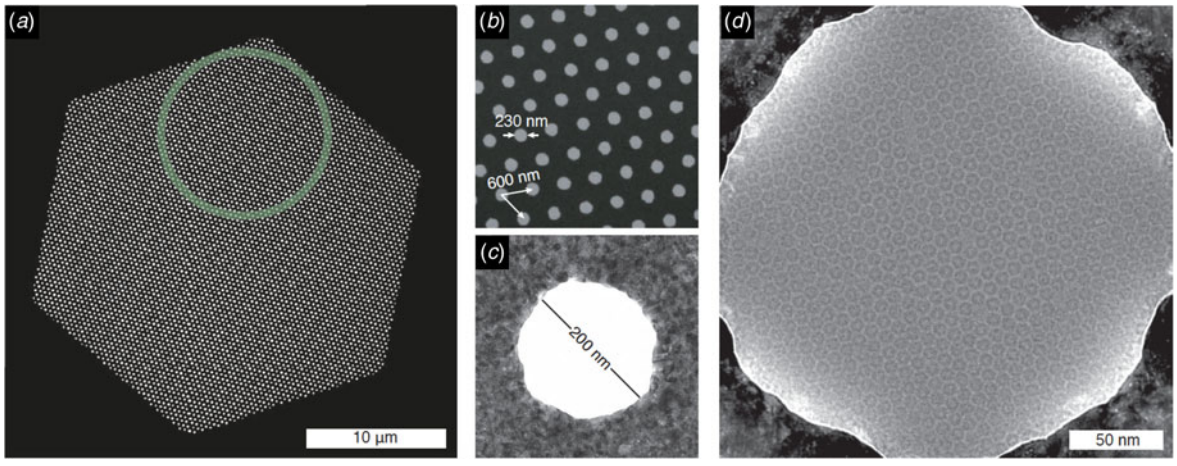


Fig. 5. All-gold specimen supports with sub-µm holes. (*a*) HexAuFoil grid support designed for movement-free cryoEM imaging. A 3 mm grid contains ~800 hexagons, each of which includes more than 5000 holes on a hexagonal lattice. The green line encircles ~800 holes. (*b*) Transmission electron micrograph of the holey gold foil, with arrows delineating the hexagonal lattice. (*c*) Micrograph of a single empty 200 nm hole. (*d*) Low-dose transmission electron micrograph of the 223 kDa DPS protein vitrified in the 260 nm holes of a HexAuFoil grid (Naydenova *et al*., 2020).

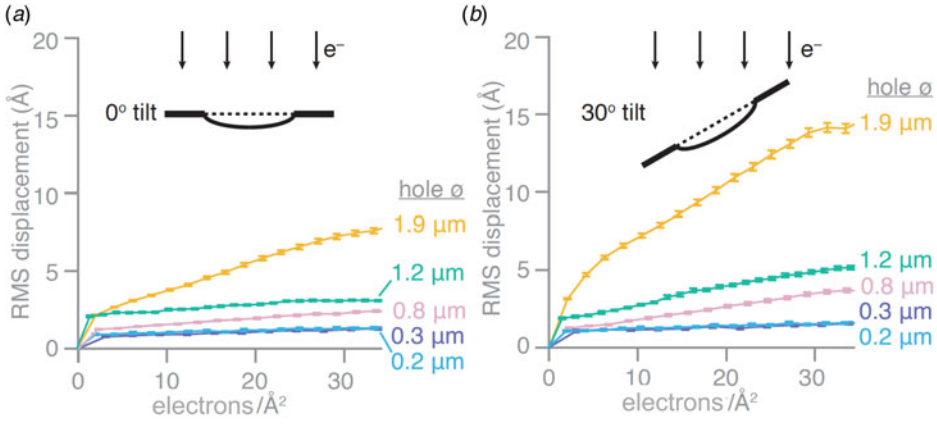


Fig. 6. Beam-induced movement depends on hole diameter. Root mean squared (RMS) displacements of gold particles in vitrified water from movies of all-gold grid holes of different diameters. Displacements are plotted as a function of cumulative electron dose for untilted specimens (*a*) and specimens tilted in the electron microscope by 30° (*b*) (Naydenova *et al*., 2020).

motion-free imaging is thus ~3300 Å, or 330 nm. The thickness of the gold foil should be similar to the desired vitreous water thickness, e.g. around 300 Å. The new supports should make it possible to take advantage of the added cryoprotection offered by liquid helium for high-resolution single-particle cryoEM.

https://doi.org/10.1017/S0033583521000020 Published online by Cambridge University Press

The structure of DPS (DNA protection during starvation), a soluble, 223 kDa protein prepared on all-gold grids with 260 nm holes, was determined at 2 Å resolution. Amplitudes and phases of structure factors that change monotonously with increasing irradiation were extrapolated to zero dose, yielding a high-resolution map and the first cryoEM structure of a pristine, undamaged protein. The absence of radiation damage was most apparent in amino acid sidechains that are known to be particularly sensitive to electron irradiation, such as aspartates and glutamates, which lose their carboxyl groups at a dose of 1–10 e Å^{-2}, and in the observation of nearby ordered water molecules (Fig. 7*a*). The relative per-frame B-factor, which should approach zero if there is no radiation damage, extrapolated to 0 Å^2 at a dose of zero electrons (Fig. 7*b*).

At a dose of 1 e Å^{-2}, or 3 MGy, radiation-sensitive sidechains appear to be still intact and water molecules in place. However, such a low dose does not produce sufficient contrast for high-resolution electron image processing, and therefore cryoEM data have to be collected at a higher total electron dose, usually around 30–40 e Å^{-2}. Note that a typical data set in X-ray protein crystallography is collected at a total dose of 1.5 MGy, equivalent to 0.5 e Å^{-2}. Even though X-rays are about 1000 times more damaging than electrons per elastic scattering event (Henderson, 1995), the damage in protein crystallography is spread out over billions of identical molecules on the crystal lattice, and therefore the molecules appear on average undamaged.

As a cautionary note, the resolution achieved with a ring-shaped heptameric bacterial light-harvesting complex on HexAuFoils (Gardiner *et al.*, 2021) was only slightly better than with conventional Quantifoil supports, most likely due to inherent flexibility of the particles. Particle flexibility and dynamics thus remain limiting, even when other limiting factors including beam-induced movement, radiation damage, particle number or particle size can be ruled out.

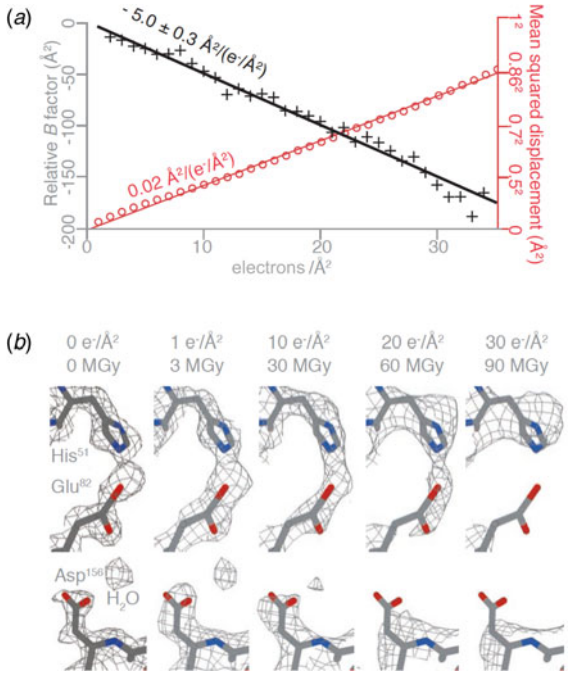


Fig. 7. Protein structure at zero electron dose. (*a*) Plot of the mean squared displacement during irradiation (red) for DPS protein particles, and relative per-frame B-factor with respect to the first frame (black), with linear fits to both. The particle displacement corresponds to diffusion with a constant of 0.02 Å^2 (e$^-$ Å^{-2})$^{-1}$ (red line). (*b*) Selected side chains and a water molecule from zero-dose extrapolated and per-frame reconstructions of DPS protein indicate progressive radiation damage. The dose is given in (e$^-$ Å^{-2}) and MGy. Residues in the refined atomic model are coloured by atom (C – grey, N – blue, O – red), and the contoured density map is shown as a mesh (Naydenova *et al.*, 2020).

Protein adsorption to the air-water interface

Once the thorny problem of beam-induced movement is resolved, the main obstacle on the way towards routine structure determination of single particles by high-resolution cryoEM is the interaction of biological macromolecules with the air-water interface.

When preparing a specimen for single-particle cryoEM, the aqueous sample solution is usually spread into a thin layer. This inevitably results in a high surface-to-volume ratio and maximizes the exposure of the particles to air. Because air is hydrophobic and proteins are amphipathic polymers, they tend to interact more or less strongly with the air-water interface. For high-resolution cryoEM, protein adsorption to the air-water interface has two drawbacks: (i) it often results in preferential particle orientation, a frequent cause of anisotropic resolution, and (ii) surface forces can disrupt the adsorbed particles partly or completely.

Protein denaturation at the air-water-interface has been studied since the 1930s (Neurath and Bull, 1938; Trurnit, 1960; Ramsden, 1994; Taylor and Glaeser, 2008; Glaeser, 2018). The process is diffusion-limited and scales roughly with protein concentration (Israelachvili, 2011). Protein complexes in the 50 kDa to 5 MDa size range (which includes most samples for single-particle cryoEM) collide with the air-water interface thousands of times every second during specimen preparation (Naydenova and Russo, 2017). Every encounter carries the risk of partial or complete denaturation. In most of the recent high-resolution cryoEM structures, only a minor fraction of a large single-particle data set contributes to the final high-resolution map. Percentages of particles used for reconstruction were 19% for the human synaptic GABAA receptor at 3.8 Å resolution (Zhu *et al.*, 2018); 15% for human P-glycoprotein at 3.4 Å (Kim and Chen, 2018); 12% for the nucleosome at 4 Å (Takizawa *et al.*, 2018); 8.9% for the 3.4 Å structure of human γ-secretase (Bai *et al.*, 2015); and only 5.7% for the 4 Å structure of a sodium channel complex from electric eel (Yan *et al.*, 2017). The remaining, up to 94% of particles were excluded from the final data set. With small proteins (less than ~150 kDa), misalignment may partly account for this high proportion of unused particles. With large complexes, damage during isolation or cryoEM grid preparation is a more likely reason. Most of this damage is probably caused by surface forces, although shear forces during blotting can also play a role (Armstrong *et al.*, 2019).

Improving sample quality

The surface activity of proteins, and hence their propensity to adhere to the air-water interface, correlates with their stability in solution (Razumovsky and Damodaran, 1999). Protein stability can be improved by adjusting buffer conditions, in particular pH and ionic strength. A data-mining study of high-resolution X-ray and cryoEM structures has found that most protein complexes are more stable at slightly acidic or basic rather than neutral pH (Chari *et al.*, 2015), and it is worth bearing this in mind when optimizing buffer conditions for cryoEM samples. At the same time, salt concentrations above 100 mM reduce image contrast, because the ions in the buffer scatter electrons more strongly

https://doi.org/10.1017/S0033583521000020 Published online by Cambridge University Press

than water. This is also true for commonly used stabilizing organic co-solutes, such as glycerol or trehalose. G-protein coupled receptors and other sensitive proteins have been stabilized by systematic mutagenesis to generate thermostable variants for crystallization and X-ray crystallography (Magnani *et al.*, 2016). Thermostable variants work equally well for cryoEM (Lee *et al.*, 2020). The same is likely to be true for other approaches that have been used to improve protein quality and stability for crystallization, e.g. removal of affinity tags, covalent modification including phosphorylation or methylation, addition of cofactors or other small molecules, addition of stabilizing antibodies or antibody fragments. The success of any such approach will depend on a massive increase in the capacity for screening cryoEM specimens, which is currently a bottleneck.

Membrane proteins are usually kept in solution by detergents, but are often more stable when reconstituted into amphipols (Tribet *et al.*, 1996; Popot, 2010; Althoff *et al.*, 2011; Liao *et al.*, 2013; Wilkes *et al.*, 2017) or lipid nanodiscs (Matthies *et al.*, 2016; Hardy *et al.*, 2018; Alvadia *et al.*, 2019; Saotome *et al.*, 2019). For soluble complexes, the detergent CHAPSO in combination with potassium chloride has helped to avoid the adsorption of soluble complexes such as bacterial RNA polymerase to the air-water interface (Chen *et al.*, 2019). For some membrane protein complexes, the same effect has been achieved with fluorinated detergents (Efremov *et al.*, 2015; Blees *et al.*, 2017; Liu *et al.*, 2017), which may compensate the protein surface charge, or form a surface monolayer that is less hydrophobic than the air-water interface itself.

Some sensitive proteins are damaged by interaction with solid surfaces long before they encounter a cryoEM grid (Rabe *et al.*, 2011; Zhou *et al.*, 2013; Lee *et al.*, 2016), and this can be a serious drawback when these proteins are purified by column chromatography or concentrated by centrifugation through a semi-permeable membrane (Joppe *et al.*, 2020). Purification or concentration steps that do not involve column chromatography or dialysis membranes, such as density gradient centrifugation or even ammonium sulphate precipitation (Hahn *et al.*, 2018), can be preferable for producing undamaged protein samples for single-particle cryoEM.

An insidious problem that is not related to sample quality or indeed specimen preparation is the inherent flexibility of a protein or its domains. Image processing cannot sort continuously flexible particles into distinct classes, and therefore the affected regions are typically of low resolution. A recent example is the cryoEM structure of the sodium/proton exchanger NHX, a eukaryotic membrane protein with a well-resolved membrane part at 3.2 Å, and a continually flexible regulatory cytoplasmic domain, for which the map resolution was only ∼15 Å (Wöhlert *et al.*, 2021). Possible solutions include attachment of specific antibodies against cytoplasmic epitopes, or of natural binding partners that might fix the domain in one or a few distinct conformations. Another option would be 3D crystallization and X-ray crystallography, hoping that crystal contacts might help to overcome domain flexibility.

Continuous support films

On the holey carbon films that are most commonly used for cryoEM specimen preparation, the sample is exposed to air on both surfaces of a hole. An obvious way around this potential problem is to prepare the sample on a continuous support film without holes that scatters electrons weakly, such as a thin film of amorphous carbon, graphene oxide or graphene. Many proteins tend to adhere to the support film, as do protein fragments, dissociated subunits or contaminants. If a protein is damaged by surface forces at the air-water interface, it may be possible to remove some or most of the denatured particles by blotting. Note that strong interaction with the support film can denature a protein, while weaker interactions result in preferential orientation, as on the air-water interface. However, the orientation distribution is likely to be different, and this can be turned into an advantage for high-resolution structure determination.

(a) Amorphous carbon films have been the standard support for biological electron microscopy at room temperature since the early 1950s (Bradley, 1954), but they have also been used for high-resolution cryoEM of soluble (Bai *et al.*, 2013; Nguyen *et al.*, 2015; Haselbach *et al.*, 2018; Jahagirdar *et al.*, 2020) and membrane protein complexes (Schraidt and Marlovits, 2011; D'Imprima *et al.*, 2017; van Pee *et al.*, 2017; Menny *et al.*, 2018; Singh *et al.*, 2020). Amorphous carbon films are inexpensive and easily prepared in the EM laboratory (Booth *et al.*, 2011). They are usually 30–50 Å thick. Proteins tend to adsorb to the carbon film, and this effect can reduce the protein concentration needed for data collection.

Depending on thickness, amorphous carbon films reduce contrast and contribute to background noise (Pantelic *et al.*, 2012), which can be problematic especially for small particles in the 50–200 kDa range. Mechanical stability (Russo and Passmore, 2016*a*, 2016*b*) and surface chemistry of amorphous carbon films, in particular hydrophobicity and surface charge (Larson *et al.*, 2011), are critical for cryoEM specimen preparation, yet notoriously difficult to control. Graphene and graphene oxide have better-defined surface properties and contribute only minimally to background noise. Both are therefore excellent, although more demanding alternatives to amorphous carbon support films.

(b) Graphene oxide is an oxygenated, hydrophilic form of graphene, in which pristine areas are interspersed with oxidized carbon (Mkhoyan *et al.*, 2009). Oxidized graphene can be chemically modified to generate functionalized surfaces for specific protein attachment (Wang *et al.*, 2020*a*, 2020*b*). Graphene oxide is typically sold as a colloidal suspension of – usually multi-layered – flakes (Bokori-Brown *et al.*, 2016; Boland *et al.*, 2017; Coscia *et al.*, 2020). The average thickness of each layer is ∼10 Å (Mkhoyan *et al.*, 2009). The flakes are easily deposited on support grids either by direct application of graphene oxide suspension (Boland *et al.*, 2017), or by floating them onto EM grids as a continuous film of graphene oxide spread on a water-methanol bath (Palovcak *et al.*, 2018). However, it is not certain that either method produces large single layers of graphene oxide reproducibly, and it is advisable to check each grid individually in the electron microscope before applying the sample. Graphene oxide introduces less background noise than amorphous carbon, as judged from the intensity of Thon rings (Pantelic *et al.*, 2010). When using graphene oxide supports, it is common to dilute the sample to nanomolar concentration, which is below the K_d of many protein complexes, which would then tend to dissociate.

(c) Graphene is a crystalline monolayer of carbon atoms. It is an excellent conductor (Geim and Novoselov, 2007) and has the highest in-plane strength of any known material (Young's modulus 1 TPa) (Lee *et al.*, 2008). Graphene is stable under a 300 kV electron beam (Sader *et al.*, 2013) and almost completely transparent to electrons in the range of interest for biological cryoEM, since the spacing of the first Bragg peak is at 2.13 Å resolution. Because graphene is a perfect single crystal, its minimal

https://doi.org/10.1017/S0033583521000020 Published online by Cambridge University Press

contribution to background noise can be removed by Fourier filtering if necessary. In principle, these desirable properties make graphene the ideal support film for cryoEM (Han *et al.*, 2020). The reasons why it has not been used more widely are twofold: (i) it is highly susceptible to surface contamination during production, handling and storage; and (ii) it is extremely hydrophobic.

Graphene is commercially available as a single-atom layer on a supporting substrate called the sacrificial layer. The sacrificial layer consists of a polymer such as polydimethylsiloxane or polymethyl methacrylate (Li *et al.*, 2009; Chen *et al.*, 2017). The sacrificial layer is removed prior to specimen preparation, which almost always results in surface contamination of the graphene film. Polymer substrates tend to leave contaminants that are resistant to organic solvents (Tripathi *et al.*, 2017) and to heating in vacuum to ~500 °C (Lin *et al.*, 2012). Even when handling pristine graphene in an inert atmosphere of N_2 or Ar/H_2, hydrocarbon contaminants can saturate the surface within 10 min, once the films are exposed to air (Pantelic *et al.*, 2012). The rate and extent of surface contamination depend on storage conditions (Naydenova *et al.*, 2019*b*). Some producers deposit graphene monolayers on a copper/gold substrate on silicon wafers (Lee *et al.*, 2013). Transfer from Cu/Au substrates yields cleaner films but requires a more laborious, multi-step procedure, during which the Cu support is dissolved in dilute $FeCl_3$ solution and gold is etched away with potassium iodide/iodine (Passmore and Russo, 2016).

Graphene can be made hydrophilic by exposure to a low-energy (10–15 eV) hydrogen plasma (Russo and Passmore, 2014*a*) that does not damage the sp^2 carbon bonds (bond energy 21 eV). Graphene can be covalently modified to produce support films with defined functionality (Liu *et al.*, 2019; Naydenova *et al.*, 2019*b*). A simpler alternative is non-covalent chemical doping (Liu *et al.*, 2012), taking advantage of π-stacking interactions between the graphene surface and polycyclic aromatic compounds, such as pyrene derivatized with polar groups (Pantelic *et al.*, 2014) (Fig. 8). When graphene films are washed with a solution of 1-pyrene carbonic acid (1-PCA), the surface becomes hydrophilic and water-soluble proteins adhere to it. By using other pyrene derivatives, the surface chemistry can be adapted to specific requirements (Pantelic *et al.*, 2014).

A cryoEM study of yeast fatty acid synthase (FAS), a 2.7 MDa soluble multi-enzyme complex, found that 90% of the particles in the holes of a standard holey carbon film were damaged at the air-water interface (D'Imprima *et al.*, 2019). The side of the particles exposed to air had unfolded locally, while the domains immersed in the aqueous phase remained intact (Fig. 9). When the complex was instead prepared on graphene monolayers doped with 1-PCA, virtually none of the particles were damaged (D'Imprima *et al.*, 2019). The phosphopantetheine transferase (PPT) domain of yeast FAS is particularly sensitive to surface denaturation, e.g. during column chromatography. When chromatography was omitted and the complex prepared for cryoEM on hydrophilized graphene supports, a 3D map at an isotropic resolution of 3.1 Å was obtained, including the fully resolved PPT domain (Joppe *et al.*, 2020).

New methods of sample deposition

In addition to protein stabilization and support films, new methods for rapid deposition of the sample on cryoEM grids are being developed to speed up grid preparation and reduce the time during which the sample is exposed to air (Fig. 10). The new preparation techniques avoid blotting the grid with filter paper (Fig. 10*a*), which not only causes mechanical stress (Armstrong *et al.*, 2019), but – depending on chemical composition – may release small amounts of Mg^{2+} and Ca^{2+} ions that can affect the structure of biological macromolecules (Walker *et al.*, 1994). The use of ashless filter paper or glass fibre filters circumvents this problem.

(a) Inkjet printing. A piezoelectric inkjet dispenser projects single, ~30 pl to 40 nl droplets with a dispense-to-plunge time of ~100–400 ms onto cryoEM grids coated with standard holey carbon film (Fig. 10*b*) (Jain *et al.*, 2012; Dandey *et al.*, 2018). The technique depends on self-wicking 'hairy grids' (Fig. 11) (Razinkov *et al.*, 2016), where grid bars are covered with a lawn of $Cu(OH)_2$ nanowires (Wei *et al.*, 2018). The nanowires absorb most of the protein solution by capillary action, leaving a thin layer of liquid in the holes that vitrifies upon immersion into liquid ethane, as usual. In a recent modification, an inkjet printing device was equipped with two piezoelectric dispensers in series (Dandey *et al.*, 2020). In this way, two solutions can be mixed on the grid as it flies past the dispenser. Inkjet printing requires sample volumes of 3–5 µl, which can be spread over dozens of grids. The wicking rate may vary from grid to grid, depending on how quickly the lawn becomes saturated, resulting in variable vitreous water layer thicknesses. The self-wicking grids are more expensive than standard grids, but they can be made in the laboratory (Wei *et al.*, 2018). A tomographic study of 46 different cryoEM samples, 32 of them prepared by inkjet printing (Noble *et al.*, 2018*a*), indicated that approximately 90% of all particles had adsorbed to the air-water interface and nearly all assumed some degree of preferential orientation. The proportion of good and bad particles for high-resolution structure determination was not assessed, but many samples showed signs of damage. Inkjet printing at current spot-to-plunge times does not prevent particle adsorption or denaturation at the air-water interface, although it does appear to alleviate preferred orientation (Noble *et al.*, 2018*b*).

In a variation of the inkjet printing technique, sample deposition onto conventional Quantifoil grids through gas-dynamic virtual nozzles yielded thin layers suitable for high-resolution structure determination (Klebl *et al.*, 2020*b*). Similar results were obtained by voltage-assisted spraying (Kontziampasis *et al.*, 2019).

(b) Aerosol spray. An aerosol of a small sample volume is sprayed from a nozzle onto the support film, shortly before the grid is vitrified (Fig. 10*c*) (Unwin and Fujiyoshi, 2012; Feng *et al.*, 2017). The technique was first applied to trap the nicotinic acetylcholine receptor channel in the open state for cryoEM (Berriman and Unwin, 1994; Unwin, 1995). By adjusting the distance between the nozzle and the liquid ethane reservoir, the plunging time can be reduced to a few ms. More recently developed systems produce aerosols by electrostatics (Kontziampasis *et al.*, 2019), surface acoustic waves (Ashtiani *et al.*, 2018) or a gas-assisted nozzle after microfluidic mixing (Maeots *et al.*, 2020). For time-resolved studies, a modified instrument uses a piezoelectric transducer for liquid atomization, allowing sample mixing about 150–100 ms before vitrification (Rubinstein *et al.*, 2019). Self-wicking grids were required, but vitrification conditions were difficult to control. A recent modification of the device places a glass fibre filter behind a conventional holey grid, which reduces cost and improves absorption capacity and reproducibility (Tan and Rubinstein, 2020). Design and software for this device

https://doi.org/10.1017/S0033583521000020 Published online by Cambridge University Press

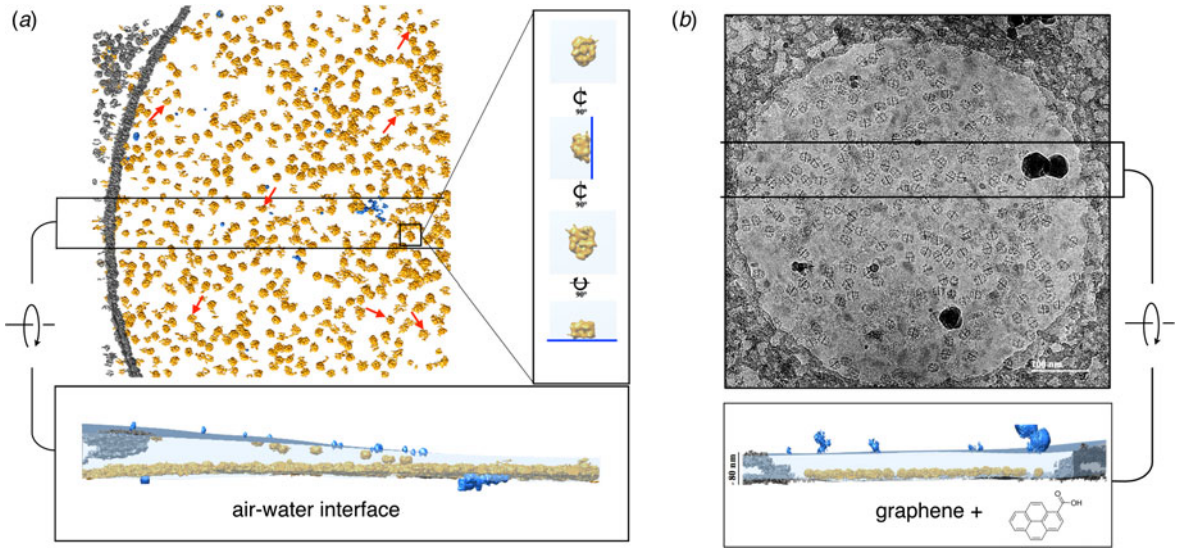


Fig. 8. Electron cryo-tomography of fatty acid synthase (FAS) on cryoEM grids. (*a*) Particle distribution of FAS particles (orange) in an unsupported vitrified buffer in a 2 µm grid hole. Red arrows indicate fragmented or damaged FAS particles. The inset shows orthogonal views of a single FAS particle distorted by adsorption to the air-water interface (blue line). A slab of the tomographic volume (below) indicates that most particles adhere to the lower meniscus. Both air-water interfaces are delineated by small contaminating ice crystals (light blue). (*b*) FAS particles on a hydrophilized graphene support. A slab of the tomographic volume indicates that all FAS particles adhere to the graphene film and are fully embedded in the ~80 nm water layer. Subsequent 3D reconstruction (not shown) yielded a 3.1 Å map of the undamaged complex (Joppe *et al*., 2020). Adapted from D'Imprima *et al*. (2019).

are freely available online, and it can be built and assembled from inexpensive materials by any mechanical workshop.

(c) Drawing with a stylus. A third method of automated cryoEM grid preparation by a device called the Vitrojet (Ravelli *et al*., 2020) uses pin-printing technology (Fig. 10*d*). Sub-nanolitre sample volumes are deposited on a standard, pre-mounted cryoEM grid (Ravelli *et al*., 2020), and drawn out with a microstylus into a thin film on a holey or continuous carbon support (Arnold *et al*., 2017). The grid is then rapidly vitrified in a jet of liquid ethane. A modified microstylus device allows for buffer exchange and sample mixing of isolated complexes or of cell extracts before deposition (Arnold *et al*., 2017, 2016). The approach has been developed further into a microfluidic method that uses magnetic beads to isolate a target protein from less than 1 µl of cell lysate and to prepare it directly for cryoEM (Schmidli *et al*., 2019). Pin-printing is still at the prototype stage but can potentially be adapted to specimen preparation for electron cryo-tomography (Nievergelt *et al*., 2019) and cryo-FIB milling (Pfeffer and Mahamid, 2018).

The three new preparation techniques spread the sample into a thin film, thus maximizing the air-water interface, although for a shorter time than standard blotting. Ideally, they reduce the amount of sample needed, and minimize the time during which it is exposed to air from minutes or seconds to a few milliseconds. The two critical time components in preparing a cryoEM specimen are (i) the time it takes to deliver the sample to the support film and (ii) the time from sample delivery to vitrification. The latter is determined by how long it takes the device to immerse the grid in liquid ethane. Currently, the shortest immersion time is 2.5 ms (Feng *et al*., 2017). Delivering the sample to the grid support before vitrification usually takes several times longer. For aerosols and inkjet printing, this includes the time of flight through air. In practice, the shortest times from bulk liquid sample to vitrification reported to date are around 6–30 ms (Klebl *et al*., 2020*a*) – two orders of magnitude slower than protein diffusion. It follows that current cryoEM specimen preparation technology cannot outrun the physics of protein diffusion in aqueous solution, and thus does not eliminate the interaction of proteins with the air-water interface.

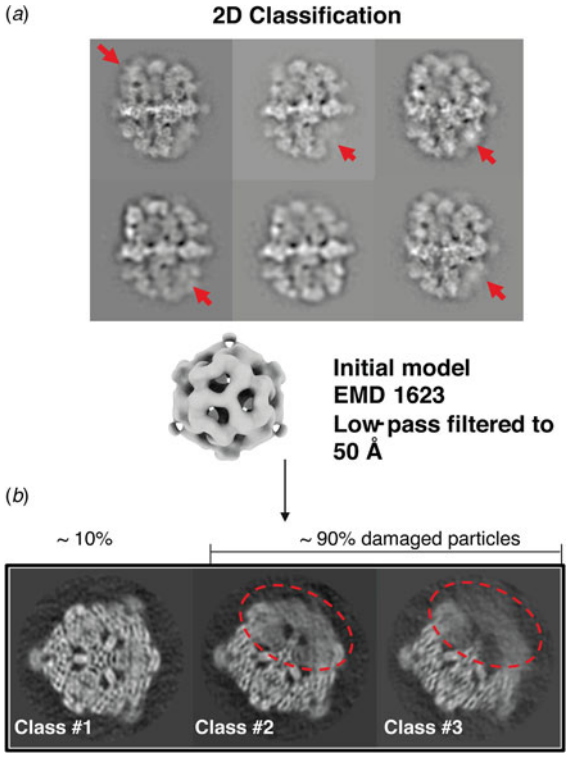


Fig. 9. Partial denaturation of FAS at the air-water interface. (*a*) Two-dimensional class averages of FAS in unsupported vitrified buffer indicate weak or distorted density in some of the six β subunits (red arrows). (*b*) Three-dimensional classification reveals partial denaturation (dashed red outline) in about 90% of all particles. The remaining ~10% (dashed grey outline) are undamaged. Adapted from D'Imprima *et al*. (2019).

https://doi.org/10.1017/S0033583521000020 Published online by Cambridge University Press

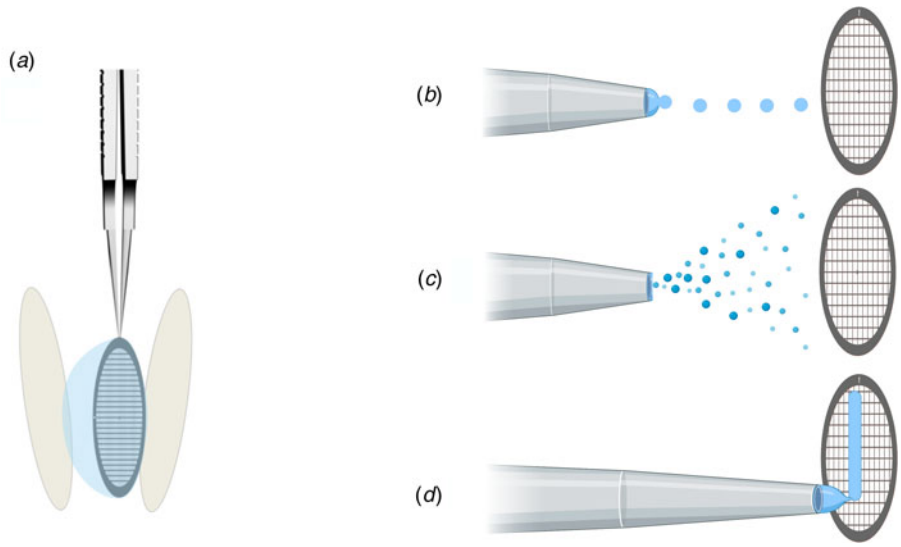


Fig. 10. [2]Methods of sample deposition. (*a*) Standard robotic plunge-freezing, e.g. in a Vitrobot. A small volume of sample solution (3 µl) is applied manually to a support grid coated with holey carbon film (Quantifoil). Excess solution is blotted off on both sides with filter paper, and the tweezers holding the grid are plunged into a reservoir of liquid ethane cooled with liquid nitrogen. (*b*) Inkjet printing, e.g. by a device known as the 'Chameleon'. Defined picolitre to nanolitre droplets are produced by a piezo-electric inkjet dispenser (Jain *et al*., 2012) and projected towards the grid, ideally a hairy grid (see Fig. 11), which is then plunge-frozen. (*c*) An aerosol of the sample solution produced by an atomizer (Berriman and Unwin, 1994; Unwin, 1995) or a microfluidic chip (Ashtiani *et al*., 2018; Kontziampasis *et al*., 2019) is emitted from a nozzle. The aerosol droplets spread on the surface of the grid, which is plunge-frozen as in (*a*). (*d*) Drawing with a stylus using pin-printing technology, e.g. by a device known as the 'Vitrojet' (Ravelli *et al*, 2020). A small sample volume is drawn out with a microstylus into a thin film on a carbon-coated grid, which is then vitrified by spraying with a jet of liquid ethane.

A systematic study (Klebl *et al*., 2020*a*) evaluates and compares the merits of inkjet printing and microfluidic spraying to standard blotting of three different, well-characterized samples: apoferritin, *Escherichia coli* ribosomes and the mitochondrial heat shock protein HSPD1. The three techniques produced grids suitable for high-resolution cryoEM data collection of all three samples, but even at the shortest preparation time of 6 ms, achieved with a microfluidics device, a significant degree of preferential orientation on the air-water interface was evident (Fig. 12). As expected, interface adsorption was most pronounced with standard blotting, which is slow. However, it turned out that this well-tried and comparatively simple technique has an unexpected advantage over the high-tech dispensers: the slow blotting process results in an up to a 30-fold increase in sample concentration near the air-water interface (Klebl *et al*., 2020*a*). For this reason, comparatively low sample concentrations are sufficient for standard blotting, whereas the faster preparation techniques require higher concentrations. The concentration effect has evidently contributed to the great success of single-particle cryoEM, in particular with samples that do not denature at the air-water interface. At present, robotic blotting produces the thinnest layers of vitrified solutions most reproducibly, which can be critical for image contrast and, hence, high resolution.

Another interesting outcome of the comparative study (Klebl *et al*., 2020*a*) was that apoferritin, *E. coli* ribosomes and the mitochondrial chaperone HSPD1 all behaved very differently with respect to interface adsorption and preferential orientation. While rapid specimen preparation can reduce the proportion of particles adsorbed to the air-water interface, the overall effect is not linear, unpredictable and very much specimen-dependent. CryoEM preparation thus needs to be optimized carefully for each sample, and at present, there is no standard procedure that would work for all.

Orientation effects were most obvious for HSPD1, which is known to interact strongly with the air-water interface (Klebl *et al*., 2020*a*), but they were also clear for ribosomes, which adhered to and oriented on the air-water interface within 13 ms. Apoferritin tended to form small clusters or rafts on the interface, but due to its high cubic symmetry, preferential orientation is less of a concern. Interaction of the protein sample with the air-water interface happened in two phases. Initial adsorption was rapid, followed by a slower phase, during which the particles orient. The interaction of HSDP1 with the interface became stronger with time, whereas it appeared to become weaker in the case of ribosomes. Overall, preferential orientation was less pronounced but still evident even with the fast dispensers, compared to blotting.

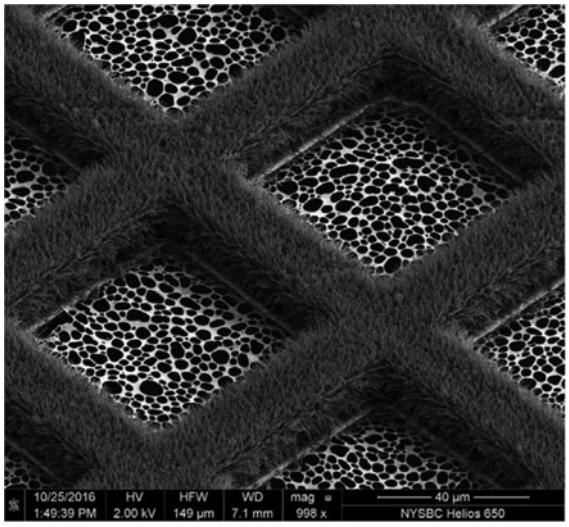


Fig. 11. Hairy grid. Scanning electron micrograph of a 300 mesh Cu/Rh grid with Cu $(OH)_2$ nanowires. The grid is coated with lacey gold film on the rhodium side. Adapted from Wei *et al*. (2018).

The particle distribution on the two opposite air-water interfaces of a support film hole was strikingly asymmetric. Often one surface was completely covered, while the opposite surface was almost empty (Fig. 13) (Klebl *et al*., 2020*a*). This was true of all three samples to a varying extent and appeared to be independent of the preparation technique. The highly asymmetric particle distribution concurs with similar findings reported previously both for blotting (D'Imprima *et al*., 2019) and inkjet printing (Noble *et al*., 2018*a*). The effect is unexplained and appears to

https://doi.org/10.1017/S0033583521000020 Published online by Cambridge University Press

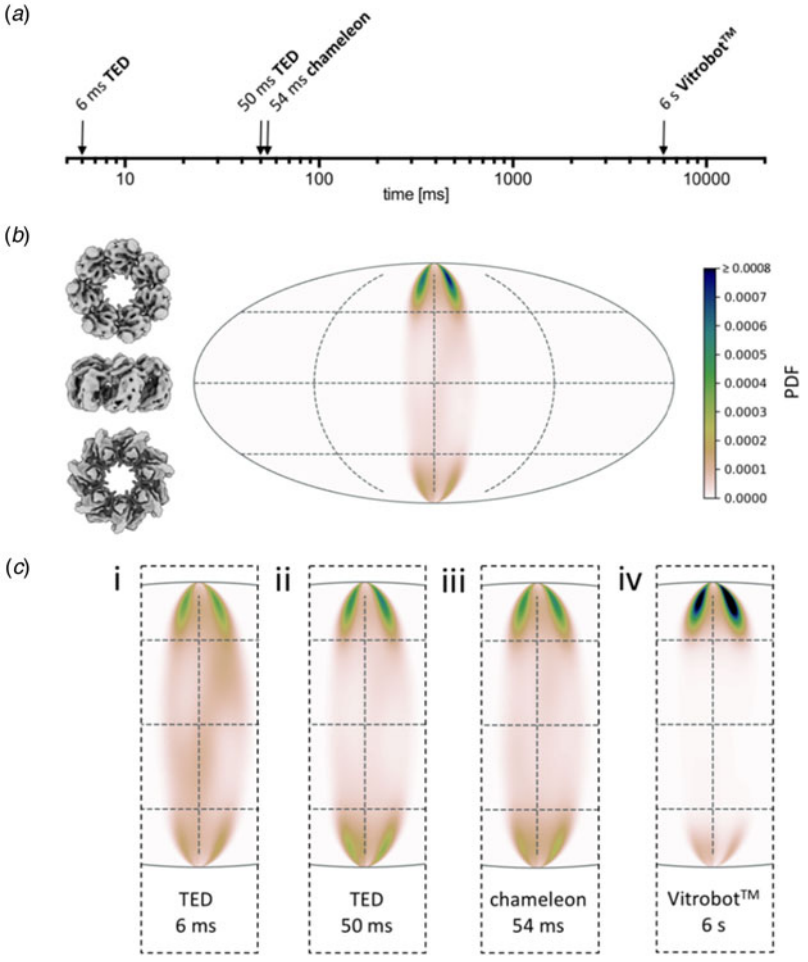


Fig. 12. Preferential orientation. Angular orientation of HSPD1 heptamer on the air-water interface at different timepoints. (*a*) Timescale of grid preparation by microfluidic spraying (TED, time-resolved cryoEM device), inkjet printing (Chameleon) or robotic blotting (Vitrobot) analysed for angular distribution. (*b*) An angular distribution map indicates a preferred orientation dominated by top views. Due to the C7 symmetry of HSDP1, only 1/7 of the area is shown. Views of the heptameric complex on the left indicate the approximate corresponding orientation. PDF, normalized probability density function indicating the probability of finding a particle in a given orientation. (*c*) Orientation distribution maps for HSPD1 prepared by microfluidic spraying within 6 ms (i) or 50 ms (ii), inkjet printing within 54 ms (iii), and robotic blotting within 6 s (iv). Adapted from Klebl *et al*. (2020*a*).

be stochastic. It may be related to local conditions on the grid that are unexplored and difficult to control, such as surface charging.

Conclusion and outlook

CryoEM has undergone a breathtaking development that few would have thought possible less than a decade ago. From an exquisitely demanding technique practised by a few experts who occasionally, and with a great deal of effort, produced high-resolution structures, it has now become a mainstay of molecular cell biology in countless laboratories around the world. CryoEM spans the wide range from single-particle protein structures at truly atomic resolution (Nakane *et al*., 2020; Yip *et al*., 2020) to large assemblies in cells and tissues investigated by electron cryo-tomography (Nievergelt *et al*., 2019), sub-tomogram averaging (Pfeffer and Mahamid, 2018) and correlative light and electron microscopy (Ganeva and Kukulski, 2020; Walter *et al*., 2020). For these reasons, cryoEM is particularly promising as a technique for the future of structural biology. Protein crystallography remains extremely powerful and is unsurpassed in terms of speed and throughput, provided that suitable crystals are available. However, protein crystallization is unpredictable and labour-intensive, and not all proteins, let alone large complexes, will crystallize. X-ray tomography is unlikely to reach a near-atomic resolution, because of radiation damage and a lack of suitable focusing optics. In cryoEM, faster cameras will speed up the process of high-resolution structure determination in the near future. More sensitive electron detectors will produce higher contrast and better resolution, and shift the boundaries towards smaller asymmetrical particles in the 30–50 kDa range, which are currently out of reach. In addition, ever more sophisticated image processing programmes that can assess and overcome particle movements and preferential orientation, or even partial denaturation are likely to be developed.

As cryoEM approaches the physical limits imposed by radiation damage and electron optics (Russo and Passmore, 2016*a*; Naydenova *et al*., 2019*a*; Peet *et al*., 2019*a*), it is now a priority to surmount the outstanding obstacles that have prevented routine high-resolution structure determination of biological macromolecules. New specimen supports or controlled devitrification have the potential of resolving the long-standing problem of beam-induced movement. Protein denaturation at the air-water interface and inherent protein flexibility then persist as the most enduring sample-related challenges. With ingenuity and additional experimentation, the promising approaches described in this review may develop into a method that works well for most biological samples. Once such methods are at hand, it will finally be possible to realize the full potential of cryoEM for routine high-resolution structure determination of biological macromolecules.

Acknowledgements. We thank Chris Russo (MRC-LMB Cambridge, UK) for communicating a manuscript prior to publication. Janet Vonck, Chris

https://doi.org/10.1017/S0033583521000020 Published online by Cambridge University Press

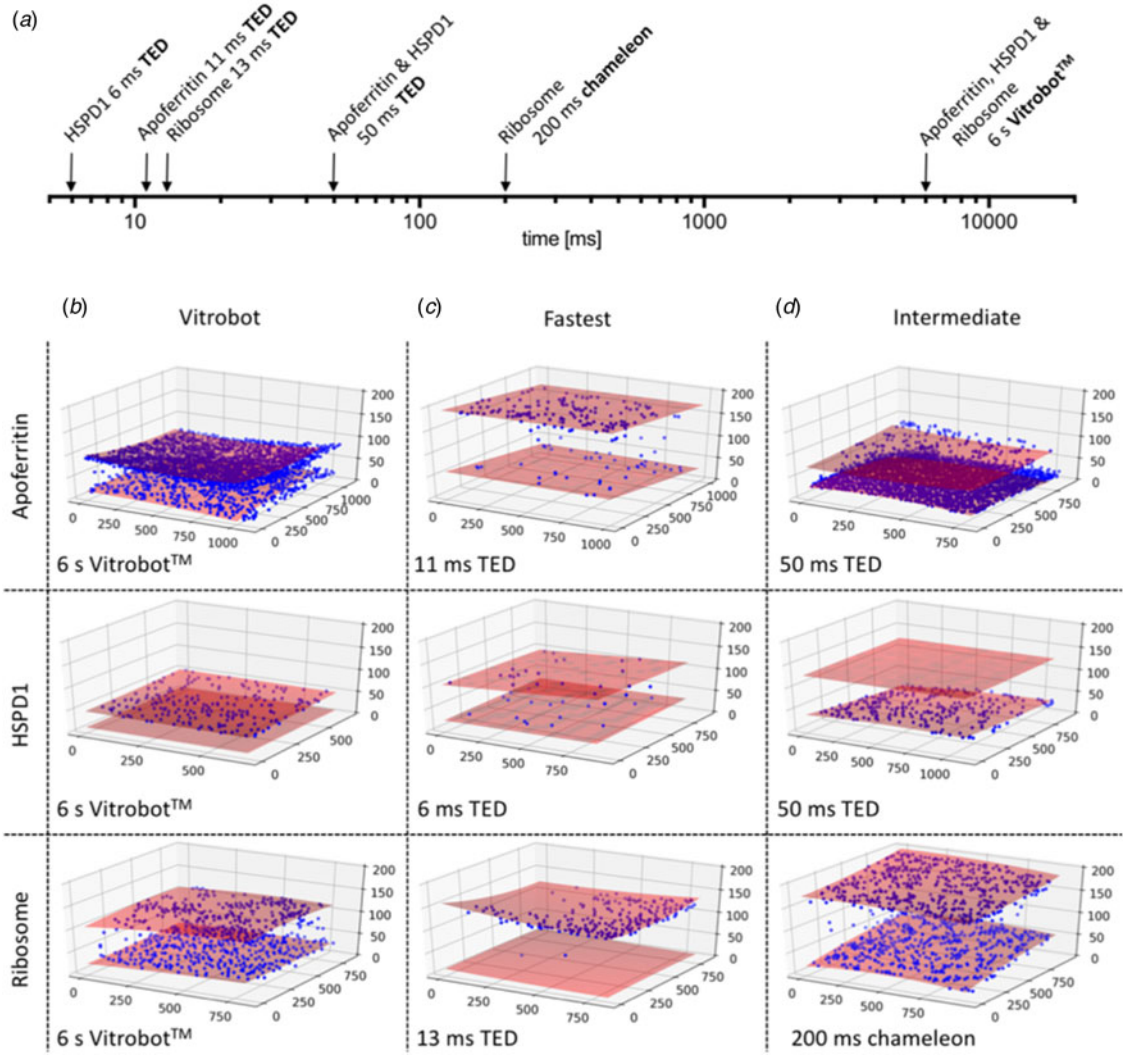


Fig. 13. CryoET of particles at the air-water interface. (*a*) Timescale of grid preparation by microfluidic spraying (TED, time-resolved cryoEM device), inkjet printing (Chameleon) or robotic blotting (Vitrobot). Representative tomograms of apoferritin, HSPD1 and ribosome grids prepared by robotic blotting with a blot time of 6 s (*b*), fast deposition within 6–13 ms by microfluidic spraying (TED; *c*) or intermediate 50–200 ms time points by microfluidic spraying (TED) or inkjet printing (Chameleon). (*d*) Red shaded areas indicate the air-water interface, and blue spheres particle location. The *x*, *y* and *z* axes indicate particle coordinates in the ice layer in nm. Adapted from Klebl *et al.* (2020*a*).

Russo, Bridget Carragher (NYSBC, New York, USA), Alex Noble (NYSBC) and Rebecca Thompson (University of Leeds, UK) contributed valuable comments. Davide Floris helped to draw Fig. 10*a*.

Financial support. Work towards this review was funded by the Max Planck Society.

Conflict of interest. None.

References

Allegretti M, Mills DJ, Mcmullan G, Kühlbrandt W and Vonck J (2014) Atomic model of the F_{420}-reducing [NiFe] hydrogenase by electron cryo-microscopy using a direct electron detector. *Elife* **3**, e01963.

Althoff T, Mills DJ, Popot J-L and Kühlbrandt W (2011) Assembly of electron transport chain components in bovine mitochondrial supercomplex I1III2IV1. *EMBO Journal* **30**, 4662–4664.

Alvadia C, Lim NK, Mosina VC, Oostergetel GT, Dutzler R and Paulino C (2019) Cryo-EM structures and functional characterization of the murine lipid scramblase TMEM16F. *Elife* **8**, e44365.

Armstrong M, Han B-G, Gomez S, Turner J, Fletcher DA and Glaeser RM (2019) Micro-scale fluid behavior during cryo-EM sample blotting. *Biophysical Journal* **118**, 708–719.

Arnold SA, Albiez S, Opara N, Chami M, Schmidli C, Bieri A, Padeste C, Stahlberg H and Braun T (2016) Total sample conditioning and preparation of nanoliter volumes for electron microscopy. *ACS Nano* **10**, 4981–4988.

Arnold SA, Albiez S, Bieri A, Syntychaki A, Adaixo R, Mcleod RA, Goldie KN, Stahlberg H and Braun T (2017) Blotting-free and lossless cryo-electron microscopy grid preparation from nanoliter-sized protein samples and single-cell extracts. *Journal of Structural Biology* **197**, 220–226.

Ashtiani D, Venugopal H, Belousoff M, Spicer B, Mak J, Neild A and De Marco A (2018) Delivery of femtolitre droplets using surface acoustic wave based atomisation for cryo-EM grid preparation. *Journal of Structural Biology* **203**, 94–101.

Bai XC, Fernandez IS, Mcmullan G and Scheres SH (2013) Ribosome structures to near-atomic resolution from thirty thousand cryo-EM particles. *Elife* **2**, e00461.

Bai XC, Yan C, Yang G, Lu P, Ma D, Sun L, Zhou R, Scheres SH and Shi Y (2015) An atomic structure of human gamma-secretase. *Nature* **525**, 212–217.

https://doi.org/10.1017/S0033583521000020 Published online by Cambridge University Press

Ben-Shem A, De Loubresse NG, Melnikov S, Jenner L, Yusupova G and Yusupov M (2011) The structure of the eukaryotic ribosome at 3.0 Å resolution. *Science* **334**, 1524–1529.

Berriman J and Unwin N (1994) Analysis of transient structures by cryo-microscopy combined with rapid mixing of spray droplets. *Ultramicroscopy* **56**, 241–252.

Blees A, Januliene D, Hofmann T, Koller N, Schmidt C, Trowitzsch S, Moeller A and Tampé R (2017) Structure of the human MHC-I peptide-loading complex. *Nature* **551**, 525–528.

Bokori-Brown M, Martin TG, Naylor CE, Basak AK, Titball RW and Savva CG (2016) Cryo-EM structure of lysenin pore elucidates membrane insertion by an aerolysin family protein. *Nature Communications* **7**, 11293.

Boland A, Martin TG, Zhang Z, Yang J, Bai XC, Chang L, Scheres SHW and Barford D (2017) Cryo-EM structure of a metazoan separase-securin complex at near-atomic resolution. *Nature Structural & Molecular Biology* **24**, 414–418.

Booth DS, Avila-Sakar A and Cheng Y (2011) Visualizing proteins and macromolecular complexes by negative stain EM: from grid preparation to image acquisition. *Journal of Visualized Experiments: JoVE* **58**, 3227.

Bradley DE (1954) Evaporated carbon films for use in electron microscopy. *British Journal of Applied Physics* **5**, 65–66.

Brilot AF, Chen JZ, Cheng A, Pan J, Harrison SC, Potter CS, Carragher B, Henderson R and Grigorieff N (2012) Beam-induced motion of vitrified specimen on holey carbon film. *Journal of Structural Biology* **177**, 630–637.

Campbell MG, Cheng A, Brilot AF, Moeller A, Lyumkis D, Veesler D, Pan J, Harrison SC, Potter CS, Carragher B and Grigorieff N (2012) Movies of ice-embedded particles enhance resolution in electron cryo-microscopy. *Structure* **20**, 1823–1828.

Chari A, Haselbach D, Kirves JM, Ohmer J, Paknia E, Fischer N, Ganichkin O, Möller V, Frye JJ, Petzold G, Jarvis M, Tietzel M, Grimm C, Peters JM, Schulman BA, Tittmann K, Markl J, Fischer U and Stark H (2015) Proteoplex: stability optimization of macromolecular complexes by sparse-matrix screening of chemical space. *Nature Methods* **12**, 859–865.

Chen M, Haddon RC, Yan R and Bekyarova E (2017) Advances in transferring chemical vapour deposition graphene: a review. *Materials Horizons* **4**, 1054–1063.

Chen J, Noble AJ, Kang JY and Darst SA (2019) Eliminating effects of particle adsorption to the air/water interface in single-particle cryo-electron microscopy: bacterial RNA polymerase and CHAPSO. *Journal of Structural Biology: X* **1**, 100005.

Cheng Y, Grigorieff N, Penczek PA and Walz T (2015) A primer to single-particle cryo-electron microscopy. *Cell* **161**, 438–449.

Coscia F, Taler-Verčič A, Chang VT, Sinn L, O'reilly FJ, Izoré T, Renko M, Berger I, Rappsilber J, Turk D and Löwe J (2020) The structure of human thyroglobulin. *Nature* **578**, 627–630.

Cyrklaff M and Kühlbrandt W (1994) High-resolution electron microscopy of biological specimens in cubic ice. *Ultramicroscopy* **55**, 141–153.

Dandey VP, Wei H, Zhang Z, Tan YZ, Acharya P, Eng ET, Rice WJ, Kahn PA, Potter CS and Carragher B (2018) Spotiton: new features and applications. *Journal of Structural Biology* **202**, 161–169.

Dandey VP, Budell WC, Wei H, Bobe D, Maruthi K, Kopylov M, Eng ET, Kahn PA, Hinshaw JE, Kundu N, Nimigean CM, Fan C, Sukomon N, Darst SA, Saecker RM, Chen J, Malone B, Potter CS and Carragher B (2020) Time-resolved cryo-EM using Spotiton. *Nature Methods* **17**, 897.–+.

D'imprima E, Salzer R, Bhaskara RM, Sanchez R, Rose I, Kirchner L, Hummer G, Kühlbrandt W, Vonck J and Averhoff B (2017) Cryo-EM structure of the bifunctional secretin complex of *Thermus thermophilus*. *Elife* **6**, e30483.

D'imprima E, Floris D, Joppe M, Sanchez R, Grininger M and Kühlbrandt W (2019) Protein denaturation at the air-water interface and how to prevent it. *Elife* **8**, e42747.

Downing KH, Mccartney MR and Glaeser RM (2004) Experimental characterization and mitigation of specimen charging on thin films with one conducting layer. *Microscopy and Microanalysis* **10**, 783–789.

Dubochet J, Lepault J, Freeman R, Berriman JA and Homo JC (1982) Electron microscopy of frozen water and aqueous solutions. *Journal of Microscopy* **128**, 219–237.

Dubochet J, Adrian M, Chang JJ, Homo JC, Lepault J, Mcdowall AW and Schultz P (1988) Cryo-electron microscopy of vitrified specimens. *Quarterly Reviews of Biophysics* **21**, 129–228.

Efremov RG, Leitner A, Aebersold R and Raunser S (2015) Architecture and conformational switch mechanism of the ryanodine receptor. *Nature* **517**, 39–43.

Feng X, Fu Z, Kaledhonkar S, Jia Y, Shah B, Jin A, Liu Z, Sun M, Chen B, Grassucci RA, Ren Y, Jiang H, Frank J and Lin Q (2017) A fast and effective microfluidic spraying-plunging method for high-resolution single-particle Cryo-EM. *Structure* **25**, 663–670.e663.

Ganeva I and Kukulski W (2020) Membrane architecture in the spotlight of correlative microscopy. *Trends in Cell Biology* **30**, 577–587.

Gardiner AT, Naydenova K, Castro-Hartmann P, Nguyen-Phan TC, Russo CJ, Sader K, Hunter CN, Cogdell RJ and Qian P (2021) The 2.4 Å cryo-EM structure of a heptameric light-harvesting 2 complex reveals two carotenoid energy transfer pathways. *Science Advances* **7**, eabe4650.

Geim AK and Novoselov KS (2007) The rise of graphene. *Nature Materials* **6**, 183–191.

Glaeser RM (2016) Specimen behavior in the electron beam. *Methods in Enzymology* **579**, 19–50.

Glaeser RM (2018) Proteins, interfaces, and cryo-EM grids. *Current Opinion in Colloid & Interface Science* **34**, 1–8.

Glaeser RM, Mcmullan G, Faruqi AR and Henderson R (2011) Images of paraffin monolayer crystals with perfect contrast: minimization of beam-induced specimen motion. *Ultramicroscopy* **111**, 90–100.

Glaeser RM, Han BG, Csencsits R, Killilea A, Pulk A and Cate JHD (2016) Factors that influence the formation and stability of thin, Cryo-EM specimens. *Biophysical Journal* **110**, 749–755.

Grant T and Grigorieff N (2015) Measuring the optimal exposure for single particle cryo-EM using a 2.6 Åreconstruction of rotavirus VP6. *Elife* **4**, e06980.

Grigorieff N, Grant T and Rohou A (2017) cisTEM: user-friendly software for single-particle image processing. *Acta Crystallographica Section A* **73**, C1368.

Guo H, Franken E, Deng Y, Benlekbir S, Singla Lezcano G, Janssen B, Yu L, Ripstein ZA, Tan YZ and Rubinstein JL (2020) Electron-event representation data enable efficient cryoEM file storage with full preservation of spatial and temporal resolution. *IUCrJ* **7**, 860–869.

Hahn A, Vonck J, Mills DJ, Meier T and Kühlbrandt W (2018) Structure, mechanism, and regulation of the chloroplast ATP synthase. *Science*, **360**, eaat4318.

Han Y, Fan X, Wang H, Zhao F, Tully CG, Kong J, Yao N and Yan N (2020) High-yield monolayer graphene grids for near-atomic resolution cryoelectron microscopy. *Proceedings of the National Academy of Sciences of the USA* **117**, 1009–1014.

Hardy D, Desuzinges Mandon E, Rothnie AJ and Jawhari A (2018) The yin and yang of solubilization and stabilization for wild-type and full-length membrane protein. *Methods* **147**, 118–125.

Haselbach D, Komarov I, Agafonov DE, Hartmuth K, Graf B, Dybkov O, Urlaub H, Kastner B, Lührmann R and Stark H (2018) Structure and conformational dynamics of the human spliceosomal B^{act} complex. *Cell* **172**, 454–464.e411.

Henderson R (1995) The potential and limitations of neutrons, electrons and X-rays for atomic resolution microscopy of unstained biological molecules. *Quarterly Reviews of Biophysics* **28**, 171–193.

Henderson R and Glaeser RM (1985) Quantitative analysis of image contrast in electron micrographs of beam-sensitive crystals. *Ultramicroscopy* **16**, 139–150.

Henderson R, Chen S, Chen JZ, Grigorieff N, Passmore LA, Ciccarelli L, Rubinstein JL, Crowther RA, Stewart PL and Rosenthal PB (2011) Tilt-pair analysis of images from a range of different specimens in single particle electron cryomicroscopy. *Journal of Molecular Biology* **413**, 1028–1046.

Israelachvili JN (2011) *Intermolecular and Surface Forces*, 3rd edn, Elsevier, Amsterdam: Academic Press.

Jahagirdar D, Jha V, Basu K, Gomez-Blanco J, Vargas J and Ortega J (2020) Alternative conformations and motions adopted by 30S ribosomal subunits visualized by cryo-electron microscopy. *RNA* **26**, 2017–2030.

Jain T, Sheehan P, Crum J, Carragher B and Potter CS (2012) Spotiton: a prototype for an integrated inkjet dispense and vitrification system for cryo-TEM. *Journal of Structural Biology* **179**, 68–75.

Joppe M, D'imprima E, Salustros N, Paithankar KS, Vonck J, Grininger M and Kuhlbrandt W (2020) The resolution revolution in cryoEM requires

https://doi.org/10.1017/S0033583521000020 Published online by Cambridge University Press

high-quality sample preparation: a rapid pipeline to a high-resolution map of yeast fatty acid synthase. *IUCrJ* **7**, 220–227.

Kim Y and Chen J (2018) Molecular structure of human P-glycoprotein in the ATP-bound, outward-facing conformation. *Science (New York, N.Y.)* **359**, 915–919.

Klebl DP, Gravett MSC, Kontziampasis D, Wright DJ, Bon RS, Monteiro DCF, Trebbin M, Sobott F, White HD, Darrow MC, Thompson RF and Muench SP (2020*a*) Need for speed: examining protein behavior during CryoEM grid preparation at different timescales. *Structure* **28**, 1238.–+.

Klebl DP, Monteiro DCF, Kontziampasis D, Kopf F, Sobott F, White HD, Trebbin M and Muench SP (2020*b*) Sample deposition onto cryo-EM grids: from sprays to jets and back. *Acta Crystallographica Section F: Structural Biology* **76**, 340–349.

Kontziampasis D, Klebl DP, Iadanza MG, Scarff CA, Kopf F, Sobott F, Monteiro DCF, Trebbin M, Muench SP and White HD (2019) A cryo-EM grid preparation device for time-resolved structural studies. *IUCrJ* **6**, 1024–1031.

Kühlbrandt W (2014) The resolution revolution. *Science* **343**, 1443–1444.

Kühlbrandt W, Wang DN and Fujiyoshi Y (1994) Atomic model of plant light-harvesting complex by electron crystallography. *Nature* **367**, 614–621.

Larson DM, Downing KH and Glaeser RM (2011) The surface of evaporated carbon films is an insulating, high-bandgap material. *Journal of Structural Biology* **174**, 420–423.

Lee C, Wei X, Kysar JW and Hone J (2008) Measurement of the elastic properties and intrinsic strength of monolayer graphene. *Science* **321**, 385–388.

Lee J, Kim Y, Shin HJ, Lee C, Lee D, Moon CY, Lim J and Chan Jun S (2013) Clean transfer of graphene and its effect on contact resistance. *Applied Physics Letters* **103**, 103104.

Lee A, Elam JW and Darling SB (2016) Membrane materials for water purification: design, development, and application. *Environmental Science-Water Research & Technology* **2**, 17–42.

Lee Y, Warne T, Nehme R, Pandey S, Dwivedi-Agnihotri H, Chaturvedi M, Edwards PC, Garcia-Nafria J, Leslie AGW, Shukla AK and Tate CG (2020) Molecular basis of beta-arrestin coupling to formoterol-bound beta(1)-adrenoceptor. *Nature* **583**, 862–866.

Li X, Zhu Y, Cai W, Borysiak M, Han B, Chen D, Piner RD, Colomba L and Ruoff RS (2009) Transfer of large-area graphene films for high-performance transparent conductive electrodes. *Nano Letters* **9**, 4359–4363.

Liao M, Cao E, Julius D and Cheng Y (2013) Structure of the TRPV1 ion channel determined by electron cryo-microscopy. *Nature* **504**, 107–112.

Lin YC, Lu CC, Yeh CH, Jin C, Suenaga K and Chiu PW (2012) Graphene annealing: how clean can it be? *Nano Letters* **12**, 414–419.

Liu J, Tang J and Gooding JJ (2012) Strategies for chemical modification of graphene and applications of chemically modified graphene. *Journal of Materials Chemistry* **22**, 12435–12452.

Liu F, Zhang Z, Csanády L, Gadsby DC and Chen J (2017) Molecular structure of the human CFTR ion channel. *Cell* **169**, 85–95.

Liu N, Zhang J, Chen Y, Liu C, Zhang X, Xu K, Wen J, Luo Z, Chen S, Gao P, Jia K, Liu Z, Peng H and Wang HW (2019) Bioactive functionalized monolayer graphene for high-resolution cryo-electron microscopy. *Journal of the American Chemical Society* **141**, 4016–4025.

Maeots ME, Lee B, Nans A, Jeong SG, Esfahani MMN, Ding S, Smith DJ, Lee CS, Lee SS, Peter M and Enchev RI (2020) Modular microfluidics enables kinetic insight from time-resolved cryo-EM. *Nature Communications* **11**, 3465.

Magnani F, Serrano-Vega MJ, Shibata Y, Abdul-Hussein S, Lebon G, Miller-Gallacher J, Singhal A, Strege A, Thomas JA and Tate CG (2016) A mutagenesis and screening strategy to generate optimally thermostabilized membrane proteins for structural studies. *Nature Protocols* **11**, 1554–1571.

Matthies D, Dalmas O, Borgnia MJ, Dominik PK, Merk A, Rao P, Reddy BG, Islam S, Bartesaghi A, Perozo E and Subramaniam S (2016) Cryo-EM structures of the magnesium channel CorA reveal symmetry break upon gating. *Cell* **164**, 747–756.

Mcmullan G, Vinothkumar KR and Henderson R (2015) Thon rings from amorphous ice and implications of beam-induced Brownian motion in single particle electron cryo-microscopy. *Ultramicroscopy* **158**, 26–32.

Menny A, Serna M, Boyd CM, Gardner S, Joseph AP, Morgan BP, Topf M, Brooks NJ and Bubeck D (2018) CryoEM reveals how the complement membrane attack complex ruptures lipid bilayers. *Nature Communications* **9**, 5316.

Mills DJ (2021) Setting up and operating a cryo-EM laboratory. *Quarterly Reviews of Biophysics* **54**, e2.

Mkhoyan KA, Contryman AW, Silcox J, Stewart DA, Eda G, Mattevi C, Miller S and Chhowalla M (2009) Atomic and electronic structure of graphene-oxide. *Nano Letters* **9**, 1058–1063.

Nakane T, Kotecha A, Sente A, Mcmullan G, Masiulis S, Brown P, Grigoras IT, Malinauskaite L, Malinauskas T, Miehling J, Uchanski T, Yu L, Karia D, Pechnikova EV, De Jong E, Keizer J, Bischoff M, Mccormack J, Tiemeijer P, Hardwick SW, Chirgadze DY, Murshudov G, Aricescu AR and Scheres SHW (2020) Single-particle cryo-EM at atomic resolution. *Nature* **587**, 152–156.

Naydenova K and Russo CJ (2017) Measuring the effects of particle orientation to improve the efficiency of electron cryomicroscopy. *Nature Communications* **8**, 629.

Naydenova K, Mcmullan G, Peet MJ, Lee Y, Edwards PC, Chen S, Leahy E, Scotcher S, Henderson R and Russo CJ (2019*a*) CryoEM at 100 keV: a demonstration and prospects. *IUCrJ* **6**, 1086–1098.

Naydenova K, Peet MJ and Russo CJ (2019*b*) Multifunctional graphene supports for electron cryomicroscopy. *Proceedings of the National Academy of Sciences of the USA* **116**, 11718–11724.

Naydenova K, Jia P and Russo CJ (2020) Cryo-EM with sub-1 A specimen movement. *Science* **370**, 223–226.

Neurath H and Bull HB (1938) The surface activity of proteins. *Chemical Reviews* **23**, 391–435.

Nguyen TH, Galej WP, Bai XC, Savva CG, Newman AJ, Scheres SH and Nagai K (2015) The architecture of the spliceosomal U4/U6.U5 tri-snRNP. *Nature* **523**, 47–52.

Nievergelt AP, Viar GA and Pigino G (2019) Towards a mechanistic understanding of cellular processes by cryoEM. *Current Opinion in Structural Biology* **58**, 149–158.

Noble AJ, Dandey VP, Wei H, Brasch J, Chase J, Acharya P, Tan YZ, Zhang Z, Kim LY, Scapin G, Rapp M, Eng ET, Rice WJ, Cheng A, Negro CJ, Shapiro L, Kwong PD, Jeruzalmi D, Georges AD, Potter CS and Carragher B (2018*a*) Routine single particle CryoEM sample and grid characterization by tomography. *Elife* **7**, e34257.

Noble AJ, Wei H, Dandey VP, Zhang Z, Tan YZ, Potter CS and Carragher B (2018*b*) Reducing effects of particle adsorption to the air–water interface in cryo-EM. *Nature Methods* **15**, 793–795.

Palovcak E, Wang F, Zheng SQ, Yu Z, Li S, Betegon M, Bulkley D, Agard DA and Cheng Y (2018) A simple and robust procedure for preparing graphene-oxide cryo-EM grids. *Journal of Structural Biology* **204**, 80–84.

Pantelic RS, Meyer JC, Kaiser U, Baumeister W and Plitzko JM (2010) Graphene oxide: a substrate for optimizing preparations of frozen-hydrated samples. *Journal of Structural Biology* **170**, 152–156.

Pantelic RS, Meyer JC, Kaiser U and Stahlberg H (2012) The application of graphene as a sample support in transmission electron microscopy. *Solid State Communications* **152**, 1375–1382.

Pantelic RS, Fu W, Schoenenberger C and Stahlberg H (2014) Rendering graphene supports hydrophilic with non-covalent aromatic functionalization for transmission electron microscopy. *Applied Physics Letters* **104**, 134103.

Passmore LA and Russo CJ (2016) Specimen preparation for high-resolution Cryo-EM. *Resolution Revolution: Recent Advances in cryoEM* **579**, 51–86.

Peet M, Henderson R and Russo CJ (2019*a*) Optimizing the electron energy for cryomicroscopy. *Microscopy and Microanalysis* **25**, 984–985.

Peet MJ, Henderson R and Russo CJ (2019*b*) The energy dependence of contrast and damage in electron cryomicroscopy of biological molecules. *Ultramicroscopy* **203**, 125–131.

Pfeffer S and Mahamid J (2018) Unravelling molecular complexity in structural cell biology. *Current Opinion in Structural Biology* **52**, 111–118.

Pfeil-Gardiner O, Mills DJ, Vonck J and Kuehlbrandt W (2019) A comparative study of single-particle cryo-EM with liquid-nitrogen and liquid-helium cooling. *IUCrJ* **6**, 1099–1105.

Popot J-L (2010) Amphipols, nanodiscs, and fluorinated surfactants: three nonconventional approaches to studying membrane proteins in aqueous solutions. *Annual Review of Biochemistry* **79**, 737–775.

https://doi.org/10.1017/S0033583521000020 Published online by Cambridge University Press

Punjani A, Rubinstein JL, Fleet DJ and Brubaker MA (2017) cryoSPARC: algorithms for rapid unsupervised cryo-EM structure determination. *Nature Methods* **14**, 290–296.

Rabe M, Verdes D and Seeger S (2011) Understanding protein adsorption phenomena at solid surfaces. *Advances in Colloid and Interface Science* **162**, 87–106.

Ramsden JJ (1994) Experimental methods for investigating protein adsorption kinetics at surfaces. *Quarterly Reviews of Biophysics* **27**, 41–105.

Ravelli RBG, Nijpels FJT, Henderikx RJM, Weissenberger G, Thewessem S, Gijsbers A, Beulen BWAMM, López-Iglesias C and Peters PJ (2020) Cryo-EM structures from sub-nl volumes using pin-printing and jet vitrification. *Nature Communications* **11**, 1–9.

Razinkov I, Dandey VP, Wei H, Zhang Z, Melnekoff D, Rice WJ, Wigge C, Potter CS and Carragher B (2016) A new method for vitrifying samples for cryoEM. *Journal of Structural Biology* **195**, 190–198.

Razumovsky L and Damodaran S (1999) Surface activity–compressibility relationship of proteins at the air–water interface. *Langmuir* **15**, 1392–1399.

Ripstein ZA and Rubinstein JL (2016) Processing of Cryo-EM movie data. *Resolution Revolution: Recent Advances in cryoEM* **579**, 103–124.

Rubinstein JL, Guo H, Ripstein ZA, Haydaroglu A, Au A, Yip CM, Di Trani JM, Benlekbir S and Kwok T (2019) Shake-it-off: a simple ultrasonic cryo-EM specimen-preparation device. *Acta Crystallographica D Structural Biology* **75**, 1063–1070.

Russo CJ and Henderson R (2018*a*) Charge accumulation in electron cryomicroscopy. *Ultramicroscopy* **187**, 43–49.

Russo CJ and Henderson R (2018*b*) Microscopic charge fluctuations cause minimal contrast loss in cryoEM. *Ultramicroscopy* **187**, 56–63.

Russo CJ and Passmore LA (2014*a*) Controlling protein adsorption on graphene for cryo-EM using low-energy hydrogen plasmas. *Nature Methods* **11**, 649–652.

Russo CJ and Passmore LA (2014*b*) Electron microscopy: ultrastable gold substrates for electron cryomicroscopy. *Science* **346**, 1377–1380.

Russo CJ and Passmore LA (2016*a*) Progress towards an optimal specimen support for electron cryomicroscopy. *Current Opinion in Structural Biology* **37**, 81–89.

Russo CJ and Passmore LA (2016*b*) Ultrastable gold substrates: properties of a support for high-resolution electron cryomicroscopy of biological specimens. *Journal of Structural Biology* **193**, 33–44.

Sader K, Stopps M, Calder LJ and Rosenthal PB (2013) Cryomicroscopy of radiation sensitive specimens on unmodified graphene sheets: reduction of electron-optical effects of charging. *Journal of Structural Biology* **183**, 531–536.

Safarian S, Hahn A, Mills DJ, Radloff M, Eisinger ML, Nikolaev A, Meier-Credo J, Melin F, Miyoshi H, Gennis RB, Sakamoto J, Langer JD, Hellwig P, Kühlbrandt W and Michel H (2019) Active site rearrangement and structural divergence in prokaryotic respiratory oxidases. *Science* **366**, 100–104.

Saotome K, Teng B, Tsui CCA, Lee WH, Tu YH, Kaplan JP, Sansom MSP, Liman ER and Ward AB (2019) Structures of the otopetrin proton channels Otop1 and Otop3. *Nature Structural & Molecular Biology* **26**, 518–525.

Schmidli C, Albiez S, Rima L, Righetto R, Mohammed I, Oliva P, Kovacik L, Stahlberg H and Braun T (2019) Microfluidic protein isolation and sample preparation for high-resolution cryo-EM. *Proceedings of the National Academy of Sciences of the USA* **116**, 15007–15012.

Schraidt O and Marlovits TC (2011) Three-dimensional model of Salmonella's needle complex at subnanometer resolution. *Science* **331**, 1192–1195.

Singh K, Graf B, Linden A, Sautner V, Urlaub H, Tittmann K, Stark H and Chari A (2020) Discovery of a regulatory subunit of the yeast fatty acid synthase. *Cell* **180**, 1130–1143.e1120.

Stark H, Zemlin F and Boettcher C (1996) Electron radiation damage to protein crystals of bacteriorhodopsin at different temperatures. *Ultramicroscopy* **63**, 75–79.

Studer D, Humbel BM and Chiquet M (2008) Electron microscopy of high pressure frozen samples: bridging the gap between cellular ultrastructure and atomic resolution. *Histochemistry and Cell Biology* **130**, 877–889.

Sun M, Azumaya C, Tse E, Frost A, Southworth D, Verba KA, Cheng Y and Agard DA (2020) Practical considerations for using K3 cameras in CDS mode for high-resolution and high-throughput single particle cryo-EM. bioRxiv, https://doi.org/10.1101/2020·1111·1108·372763.

Takizawa Y, Tanaka H, Machida S, Koyama M, Maehara K, Ohkawa Y, Wade PA, Wolf M and Kurumizaka H (2018) Cryo-EM structure of the nucleosome containing the ALB1 enhancer DNA sequence. *Open Biology* **8**, 170255.

Tan YZ and Rubinstein JL (2020) Through-grid wicking enables high-speed cryoEM specimen preparation. *Acta Crystallographica. Section D, Structural Biology* **76**, 1092–1103.

Taylor KA and Glaeser RM (2008) Retrospective on the early development of cryoelectron microscopy of macromolecules and a prospective on opportunities for the future. *Journal of Structural Biology* **163**, 214–223.

Thorne RE (2020) Hypothesis for a mechanism of beam-induced motion in cryo-electron microscopy. *IUCrJ* **7**, 416–421.

Tribet C, Audebert R and Popot J-L (1996) Amphipols: polymers that keep membrane proteins soluble in aqueous solutions. *Proceedings of the National Academy of Sciences of the USA* **93**, 15047–15050.

Tripathi M, Mittelberger A, Mustonen K, Mangler C, Kotakoski J, Meyer JC and Susi T (2017) Cleaning graphene: comparing heat treatments in air and in vacuum. *Physica Status Solidi-Rapid Research Letters* **11**, 1700124.

Trurnit HJ (1960) A theory and method for the spreading of protein monolayers. *Journal of Colloid Science* **15**, 1–13.

Unwin N (1995) Acetylcholine receptor channel imaged in the open state. *Nature* **373**, 37–43.

Unwin N and Fujiyoshi Y (2012) Gating movement of acetylcholine receptor caught by plunge-freezing. *Journal of Molecular Biology* **422**, 617–634.

Van Pee K, Neuhaus A, D'imprima E, Mills DJ, Kühlbrandt W and Yildiz O (2017) CryoEM structures of membrane pore and prepore complex reveal cytolytic mechanism of Pneumolysin. *Elife* **6**, e23644.

Vinothkumar KR and Henderson R (2016) Single particle electron cryomicroscopy: trends, issues and future perspective. *Quarterly Reviews of Biophysics* **49**, e13.

Vinothkumar KR, Mcmullan G and Henderson R (2014) Molecular mechanism of antibody-mediated activation of beta-galactosidase. *Structure* **22**, 621–627.

Walker M, White H, Belknap B and Trinick J (1994) Electron cryomicroscopy of acto-myosin-S1 during steady-state ATP hydrolysis. *Biophysical Journal* **66**, 1563–1572.

Walter A, Paul-Gilloteaux P, Plochberger B, Sefc L, Verkade P, Mannheim JG, Slezak P, Unterhuber A, Marchetti-Deschmann M, Ogris M, Buhler K, Fixler D, Geyer SH, Weninger WJ, Glosmann M, Handschu S and Wanek T (2020) Correlated multimodal imaging in life sciences: expanding the biomedical horizon. *Frontiers of Physics* **8**, 47.

Wang F, Liu Y, Yu Z, Li S, Feng S, Cheng Y and Agard DA (2020*a*) General and robust covalently linked graphene oxide affinity grids for high-resolution cryo-EM. *Proceedings of the National Academy of Sciences of the USA* **117**, 24269–24273.

Wang F, Yu Z, Betegon M, Campbell MG, Aksel T, Zhao J, Li S, Douglas SM, Cheng Y and Agard DA (2020*b*) Amino and PEG-amino graphene oxide grids enrich and protect samples for high-resolution single particle cryo-electron microscopy. *Journal of Structural Biology* **209**, 107437.

Wei H, Dandey VP, Zhang Z, Raczkowski A, Rice WJ, Carragher B and Potter CS (2018) Optimizing 'self-wicking' nanowire grids. *Journal of Structural Biology* **202**, 170–174.

Wieferig J-P, Mills D and Kühlbrandt W (2021) Devitrification reduces beam-induced movement in cryo-EM. *IUCrJ* **8**(2), 186–194.

Wilkes M, Madej MG, Kreuter L, Rhinow D, Heinz V, De Sanctis S, Ruppel S, Richter RM, Joos F, Grieben M, Pike AC, Huiskonen JT, Carpenter EP, Kühlbrandt W, Witzgall R and Ziegler C (2017) Molecular insights into lipid-assisted Ca(2+) regulation of the TRP channel Polycystin-2. *Nature Structural & Molecular Biology* **24**, 123–130.

Wöhlert D, Yildiz Ö and Kühlbrandt W (2021) Structure, mechanism and regulation of two eukaryotic Na+/H+ exchangers. Manuscript submitted.

Yan Z, Zhou Q, Wang L, Wu J, Zhao Y, Huang G, Peng W, Shen H, Lei J and Yan N (2017) Structure of the Nav1·4-β1 complex from electric eel. *Cell* **170**, 470–482.e411.

Yip KM, Fischer N, Paknia E, Chari A and Stark H (2020) Atomic-resolution protein structure determination by cryo-EM. *Nature* **587**, 157–161.

https://doi.org/10.1017/S0033583521000020 Published online by Cambridge University Press

Zheng SQ, Palovcak E, Armache JP, Verba KA, Cheng Y and Agard DA (2017) Motioncor2: anisotropic correction of beam-induced motion for improved cryo-electron microscopy. *Nature Methods* **14**, 331–332.

Zhou X, Zhang Y, Zhang F, Pillai S, Liu J, Li R, Dai B, Li B and Zhang Y (2013) Hierarchical ordering of amyloid fibrils on the mica surface. *Nanoscale* **5**, 4816–4822.

Zhu S, Noviello CM, Teng J, Walsh RM, Kim JJ and Hibbs RE (2018) Structure of a human synaptic GABAA receptor. *Nature* **559**, 67–72.

Zivanov J, Nakane T, Forsberg BO, Kimanius D, Hagen WJH, Lindahl E and Scheres SHW (2018) New tools for automated high-resolution cryo-EM structure determination in RELION-3. *Elife* **7**, e42166.

https://doi.org/10.1017/S0033583521000020 Published online by Cambridge University Press